Journal of Engineering Mathematics (2005) 53: 359–383
DOI 10.1007/s10665-005-9020-3

Lubrication models with small to large slip lengths

A. MÜNCH[1], B. WAGNER[1] and T.P. WITELSKI[2]
[1] *Weierstrass Institute for Applied Analysis and Stochastics, Mohrenstraße 39, 10117 Berlin, Germany (E-mail: muench@mathematik.hu-berlin.de, wagnerb@wias-berlin.de);* [2] *Department of Mathematics, Duke University, Durham, NC 27708-0320, USA (E-mail: witelski@math.duke.edu)*

Received 17 June 2005; accepted in revised form 30 August 2005

Abstract. A set of lubrication models for the thin film flow of incompressible fluids on solid substrates is derived and studied. The models are obtained as asymptotic limits of the Navier-Stokes equations with the Navier-slip boundary condition for different orders of magnitude for the slip-length parameter. Specifically, the influence of slip on the dewetting behavior of fluids on hydrophobic substrates is investigated here. Matched asymptotics are used to describe the dynamic profiles for dewetting films and comparison is given with computational simulations. The motion of the dewetting front shows transitions from being nearly linear in time for no-slip to $t^{2/3}$ as the slip is increased. For much larger slip lengths the front motion appears to become linear again. Correspondingly, the dewetting profiles undergo a transition from oscillatory to monotone decay into the uniform film layer for large slip. Increasing the slip further, to very large values, is associated with an increasing degree of asymmetry in the structure of the dewetting ridge profile.

Key words: dewetting films, lubrication models, matched asymptotics, Navier-slip condition, stability analysis

1. Introduction

Lubrication models have shown to be extremely useful approximations to the full Navier-Stokes equations for investigating the dynamics of thin liquid films, including the motion and instabilities of their contact lines [1]. For film thicknesses in the range of a few micrometers and larger, the choice of the boundary condition at the solid substrate enters only weakly in that it does not influence the eventual appearance of instabilities, such as formation of fingers at the three-phase contact-line; see for example [2–5]. For other applications, such as for the dewetting of a nano-scale thin polymer film on a hydrophobic substrate the boundary condition at the substrate appears to have a crucial influence on the dynamics and morphology of the film. Experimental studies of unstable thin films coating solids have shown significant differences in the patterns that develop when fluid instabilities lead to the formation of growing "dry regions" on the solid. In this context the occurrence and nature of slippage of the liquid film on the solid substrate is of large interest, not only for fundamental research, see *e.g.* [6–10], but also for technological applications such as microfluidic devices.

We examine the influence of the fluid-solid interface using lubrication models that include both an intermolecular potential and slippage to represent the chemical and molecular-scale physical properties of the solid. The models are obtained as asymptotic limits of the Navier-Stokes equations with the Navier-slip boundary condition for different orders of magnitude for the slip-length parameter. The slip-length B can be understood as an off-set length such that the fluid velocity at the solid surface is given by the slip-length times the normal derivative of the velocity,

$$U(Z=0) = B\partial_Z U(Z=0). \tag{1.1}$$

For flows of Newtonian fluids on smooth rigid surfaces, the classic no-slip boundary condition, $U(Z=0)=0$, corresponds to zero slip length. Positive slip lengths have been used to model many different physical systems, including effects such as surface roughness and non-Newtonian fluid properties, see *e.g.* the recent review [11].

We obtain closed-form lubrication models over a wide range of slip lengths. Particular asymptotic scalings for the slip lead to two distinguished limits that we call the equations for the *weak slip* and *strong slip* regimes, respectively. For other choices of slip scalings, these models will be shown to reduce to other models that have been used in different parts of fluid dynamics.

For these models we focus on describing the growth of dewetted regions in the film. In experiments, these regions grow as circles until secondary instabilities step in. Fluid transported out of the growing dry regions collects in a ridge profile that advances into the undisturbed fluid; see Figure 1. We show that the axisymmetric profile can be analyzed within a one-dimensional thin-film model. Matched asymptotic expansions are used to determine its speed and structure.

We show that for the weak-slip regime the motion of the dewetting front changes from an almost constant speed (apart from logarithmic corrections) to position $\propto t^{2/3}$ as slip increases. Meanwhile, in the strong-slip regime, increasing the slip length appears to cause the reverse behavior, *i.e.*, increasing slip increases the scaling exponent for the front position.

We also show that for the strong-slip regime the ridge morphology changes from a damped oscillating structure behind the ridge and towards the undisturbed film, to a monotone decaying structure, as the slip length is increased. For even larger slip lengths, the exponential decay rate decreases and the ridge profiles show a pronounced asymmetry. We use linear stability analysis to derive the critical slip length for the transition and compare this to the numerical solution of the strong-slip lubrication model. This property of the strong-slip lubrication model captures the recently experimentally observed morphological transition of the ridge when the liquid/solid friction was altered [12].

2. Derivation of the lubrication-slip equations

2.1. Governing equations

We begin from the Navier-Stokes equations for the flow of a viscous incompressible fluid layer on $0 \le Z \le H(X,T)$ in two dimensions with

$$\rho\,(\partial_T \mathbf{U} + \mathbf{U}\cdot\nabla\mathbf{U}) = -\nabla(P + F'(H)) + \mu\nabla^2\mathbf{U}, \qquad \nabla\cdot\mathbf{U} = 0. \tag{2.1}$$

Here, $\mathbf{U} = U(X,Z,T)\mathbf{i} + W(X,Z,T)\mathbf{k}$ denotes the velocity field, $P = P(X,Z,T)$ the pressure field, and $F'(H) = dF/dH$ the contribution due to an intermolecular potential $F(H)$ (of Born/Van der Waals type).

At the free surface $Z = H(X,T)$, we have the usual kinematic and stress boundary conditions and constant surface tension σ. For flow over a uniform solid substrate, we consider the

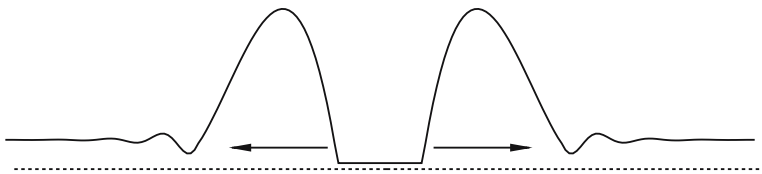

Figure 1. Sketch of the cross-section of a dewetting film after rupture, showing the expanding dewetted residual layer (also called a "hole" or "dry spot") in the middle and the adjacent "dewetting ridges" moving into the surrounding undisturbed uniform film.

Navier-slip boundary condition at $Z=0$,

$$U = B\,\partial_Z U. \tag{2.2}$$

For the scaling for nondimensionalization we use

$$\begin{aligned} Z &= \mathbb{H} z, \quad X = \mathbb{L} x, \quad H = \mathbb{H} h, \quad B = \mathbb{H} b, \\ U &= \mathbb{U} u, \quad W = \mathbb{W} w, \quad T = \tfrac{\mathbb{H}}{\mathbb{W}} t, \quad P + F' = \mathbb{P} p, \quad F' = \mathbb{P}\phi'. \end{aligned} \tag{2.3}$$

For the lubrication models we will derive, it is slightly more convenient to choose the dimensionless pressure so that it includes the contribution from the intermolecular forces. Assume also

$$\frac{\mathbb{H}}{\mathbb{L}} = \frac{\mathbb{W}}{\mathbb{U}} = \epsilon \quad \text{and} \quad \epsilon \ll 1. \tag{2.4}$$

Then, we write the governing equations in dimensionless form as

$$\epsilon \frac{\rho \mathbb{U}\mathbb{H}}{\mu}(\partial_t u + u\partial_x u + w\partial_z u) = -\epsilon \frac{\mathbb{P}\mathbb{H}}{\mu\mathbb{U}}\partial_x p + \epsilon^2 \partial_{xx} u + \partial_{zz} u, \tag{2.5a}$$

$$\epsilon^2 \frac{\rho \mathbb{U}\mathbb{H}}{\mu}(\partial_t w + u\partial_x w + w\partial_z w) = -\frac{\mathbb{P}\mathbb{H}}{\mu\mathbb{U}}\partial_z p + \epsilon^3 \partial_{xx} w + \epsilon \partial_{zz} w, \tag{2.5b}$$

$$\partial_x u + \partial_z w = 0. \tag{2.5c}$$

For the boundary conditions at $z = h(x,t)$ the tangential and normal stress and the kinematic condition respectively are,

$$\left(\partial_z u + \epsilon^2 \partial_x w\right)\left(1 - \epsilon^2 (\partial_x h)^2\right) + 2\epsilon^2 \partial_x h\,(\partial_z w - \partial_x u) = 0, \tag{2.6a}$$

$$\begin{aligned} p - \phi'(h) - 2\epsilon \frac{\mu\mathbb{U}}{\mathbb{P}\mathbb{H}} \frac{\left(1 - \epsilon^2(\partial_x h)^2\right)\partial_z w - \partial_x h\left(\partial_z u + \epsilon^2 \partial_x w\right)}{1 + \epsilon^2 (\partial_x h)^2} \\ + \epsilon^2 \frac{\sigma}{\mathbb{P}\mathbb{H}} \frac{\partial_{xx} h}{\left(1 + \epsilon^2 (\partial_x h)^2\right)^{3/2}} = 0, \end{aligned} \tag{2.6b}$$

$$\partial_t h - w + u\partial_x h = 0. \tag{2.6c}$$

For the boundary conditions at $z = 0$ we have the impermeability and slip condition

$$w = 0 \quad \text{and} \quad u = b\,\partial_z u. \tag{2.7}$$

The asymptotic regimes we will derive next are all characterized by the orders of magnitude of the slip length. As one traverses the ranges of the slip length, the flow field will change from a parabolic flow field to what is essentially plug flow; see Figure 2. This implies a change from the balance of the pressure gradient with the dominant viscosity contribution in the horizontal momentum equation to the balance of the pressure gradient and viscosity contribution in the vertical momentum equation, and thereby also a change of the velocity scale.

2.2. Weak-slip regime

Following the usual approach for low-Reynolds-number lubrication theory, we balance the pressure gradient with the dominant viscous term in the horizontal momentum balance in (2.5a) to yield the scaling

$$\frac{\mathbb{P}\mathbb{H}}{\mu\mathbb{U}} \sim \epsilon^{-1}.$$

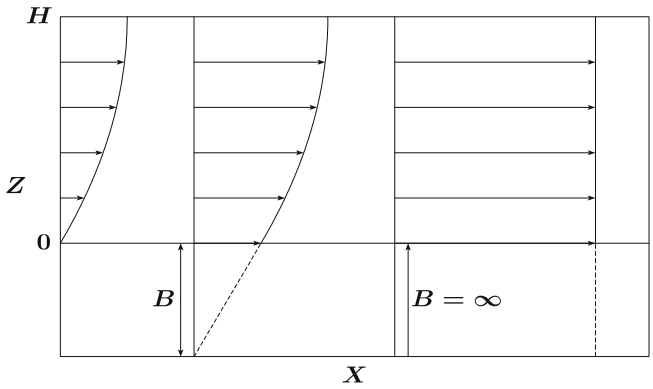

Figure 2. The left curve shows the parabolic flow profile for the no-slip situation. The curve in the middle is the profile for partial slip with a finite slip length, indicated by B. The curve on the right shows the profile for plug flow when the effective slip length becomes infinite.

We also assume surface tension to play a role throughout, *i.e.*, by using (2.6b)

$$\frac{\sigma}{\mathbb{P}\,\mathbb{H}} \sim \epsilon^{-2}.$$

These balances yield a pressure and velocity scale and a relation to the capillary number

$$\mathbb{U} = \frac{\sigma\epsilon^3}{\mu} \quad \text{and} \quad \mathrm{Ca} = \frac{\mu\mathbb{U}}{\sigma} = \epsilon^3. \tag{2.8}$$

We also write the Reynolds number as

$$\mathrm{Re} = \frac{\rho\mathbb{U}\,\mathbb{H}}{\mu} = \epsilon^3 \frac{\rho\sigma\mathbb{H}}{\mu^2} = \epsilon^3 \mathrm{Re}^*, \tag{2.9}$$

where Re^* is the reduced Reynolds number, assumed to be O(1). The nondimensional problem for the weak-slip regime is therefore

$$\epsilon^4 \mathrm{Re}^* \left(\partial_t u + u\partial_x u + w\partial_z u\right) = -\partial_x p + \epsilon^2 \partial_{xx} u + \partial_{zz} u, \tag{2.10a}$$

$$\epsilon^6 \mathrm{Re}^* \left(\partial_t w + u\partial_x w + w\partial_z w\right) = -\partial_z p + \epsilon^4 \partial_{xx} w + \epsilon^2 \partial_{zz} w, \tag{2.10b}$$

$$\partial_x u + \partial_z w = 0, \tag{2.10c}$$

with boundary conditions at $z = h(x,t)$,

$$\left(\partial_z u + \epsilon^2 \partial_x w\right)\left(1 - \epsilon^2 (\partial_x h)^2\right) + 2\epsilon^2 \partial_x h \left(\partial_z w - \partial_x u\right) = 0, \tag{2.11a}$$

$$p - \phi'(h) - 2\epsilon^2 \frac{\left(1 - \epsilon^2(\partial_x h)^2\right)\partial_z w - \partial_x h\left(\partial_z u + \epsilon^2 \partial_x w\right)}{1 + \epsilon^2 (\partial_x h)^2} + \frac{\partial_{xx} h}{\left(1 + \epsilon^2 (\partial_x h)^2\right)^{3/2}} = 0, \tag{2.11b}$$

$$\partial_t h - w + u\,\partial_x h = 0, \tag{2.11c}$$

and boundary condition at $z = 0$,

$$w = 0 \quad \text{and} \quad u = b\,\partial_z u. \tag{2.12}$$

The leading-order problem is

$$\partial_x p = \partial_{zz} u, \quad \partial_z p = 0, \quad \partial_x u + \partial_z w = 0, \tag{2.13a,b,c}$$

with boundary conditions

$$\partial_z u = 0, \quad p = -\partial_{xx} h + \phi'(h), \quad \partial_t h = w - u\partial_x h \quad \text{at} \quad z = h(x,t), \tag{2.14a}$$

$$w = 0 \quad \text{and} \quad u = b\,\partial_z u \quad \text{at} \quad z = 0. \tag{2.14b}$$

As is well known, see *e.g.* [1, 13], one can integrate the problem (2.13a)–(2.14b) with respect to z to obtain a single, dimension-reduced lubrication equation for the profile $h(x,t)$:

$$\partial_t h = -\partial_x \left[\left(\tfrac{1}{3} h^3 + b h^2 \right) \partial_x \left(\partial_{xx} h - \phi'(h) \right) \right]. \tag{2.15}$$

2.3. Strong-slip regime

There is another regime which arises, for example in the context of microfluidics, where the dynamics of polymer films with thickness on the nano- to micro-meter scale is strongly influenced by the slip length, which in turn can be larger than the thickness of the film.

Here, we similarly balance pressure with the dominant viscous term, but now the leading-order balance occurs in the vertical momentum balance in (2.5b), which yields the scaling

$$\frac{\mathbb{P}\,\mathbb{H}}{\mu\,\mathbb{U}} \sim \epsilon.$$

As in the weak-slip regime, we also assume that surface tension and pressure balance in the normal stress condition, *i.e.*, $\sigma/(\mathbb{P}\,\mathbb{H}) \sim \epsilon^{-2}$. We obtain the same expression for the pressure scale but much larger scales for the velocity scale and the capillary number

$$\mathbb{U} = \frac{\sigma\epsilon}{\mu} \quad \text{and} \quad \mathrm{Ca} = \frac{\mu\mathbb{U}}{\sigma} = \epsilon; \tag{2.16}$$

see (2.11) for comparison. The Reynolds number is

$$\mathrm{Re} = \frac{\rho\mathbb{U}\,\mathbb{H}}{\mu} = \epsilon\frac{\rho\sigma\mathbb{H}}{\mu^2} = \epsilon\mathrm{Re}^*. \tag{2.17}$$

The nondimensional problem for the strong-slip regime is therefore

$$\epsilon^2\mathrm{Re}^*\,(\partial_t u + u\partial_x u + w\partial_z u) = -\epsilon^2\partial_x p + \epsilon^2\partial_{xx} u + \partial_{zz} u, \tag{2.18a}$$

$$\epsilon^2\mathrm{Re}^*\,(\partial_t w + u\partial_x w + w\partial_z w) = -\partial_z p + \epsilon^2\partial_{xx} w + \partial_{zz} w, \tag{2.18b}$$

$$\partial_x u + \partial_z w = 0, \tag{2.18c}$$

with boundary conditions at $z = h(x,t)$,

$$\left(\partial_z u + \epsilon^2\partial_x w\right)\left(1 - \epsilon^2(\partial_x h)^2\right) + 2\epsilon^2\partial_x h\,(\partial_z w - \partial_x u) = 0, \tag{2.19a}$$

$$p - \phi'(h) - 2\frac{\left(1 - \epsilon^2(\partial_x h)^2\right)\partial_z w - \partial_x h\left(\partial_z u + \epsilon^2\partial_x w\right)}{1 + \epsilon^2(\partial_x h)^2} + \frac{\partial_{xx} h}{\left(1 + \epsilon^2(\partial_x h)^2\right)^{3/2}} = 0, \tag{2.19b}$$

$$\partial_t h - w + u\,\partial_x h = 0, \tag{2.19c}$$

and boundary condition at $z = 0$:

$$w = 0 \quad \text{and} \quad u = b\,\partial_z u. \tag{2.20}$$

While in the weak-slip regime, b was assumed to be O(1), we will discuss here the admissible orders of magnitude for the strong-slip regime.

We begin by assuming that u, w, p and h have the asymptotic expansions

$$u(x,z,t;\epsilon)=u_0(x,z,t)+\epsilon^2 u_1(x,z,t)+\mathrm{O}(\epsilon^4), \tag{2.21a}$$
$$w(x,z,t;\epsilon)=w_0(x,z,t)+\epsilon^2 w_1(x,z,t)+\mathrm{O}(\epsilon^4), \tag{2.21b}$$
$$p(x,z,t;\epsilon)=p_0(x,z,t)+\epsilon^2 p_1(x,z,t)+\mathrm{O}(\epsilon^4), \tag{2.21c}$$
$$h(x,t;\epsilon)=h_0(x,t)+\epsilon^2 h_1(x,t)+\mathrm{O}(\epsilon^4). \tag{2.21d}$$

To leading order in ϵ we have the problem

$$\partial_{zz}u_0=0, \quad \partial_z p_0=\partial_{zz}w_0, \quad \partial_x u_0+\partial_z w_0=0, \tag{2.22a,b,c}$$

with boundary conditions at $z=h_0(x,t)$:

$$\partial_z u_0=0, \quad p_0-\phi'(h_0)-2\,(\partial_z w_0-\partial_x h_0\partial_z u_0)+\partial_{xx}h_0=0, \tag{2.23a,b}$$
$$\partial_t h_0-w_0+u_0\,\partial_x h_0=0, \tag{2.23c}$$

and boundary conditions at $z=0$:

$$w_0=0 \quad \text{and} \quad \partial_z u_0=\frac{u_0}{b}. \tag{2.24}$$

From (2.23a), the leading-order horizontal velocity is independent of z:

$$u_0\equiv u_0(x,t). \tag{2.25}$$

From (2.22c) and $(2.24)_1$ we find

$$w_0=-z\,\partial_x u_0, \tag{2.26}$$

and from (2.23b)

$$p_0-\phi'(h_0)=-\,\partial_{xx}h_0-2\,\partial_x u_0\,. \tag{2.27}$$

If $b=\mathrm{O}(1)$ then $(2.24)_2$ would imply that $u_0=0$ and $w_0=0$ and hence $\partial_t h_0=0$. We need to assume that the slip length $b\gg\mathrm{O}(1)$ in order to capture the nontrivial dynamics. Hence, we let

$$b=\frac{\beta}{\epsilon^\alpha}, \quad \text{so that} \quad \partial_z u_0=\frac{\epsilon^\alpha}{\beta}u_0 \quad \text{with} \quad \alpha>0. \tag{2.28}$$

To leading order $(2.24)_2$ then becomes $\partial_z u_0=0$ and is compatible with (2.23a). In order to determine $u_0(x,t)$ we need to make use of the next-order correction,

$$\mathrm{Re}^*\,(\partial_t u_0+u_0\partial_x u_0)=-\partial_x p_0+\partial_{xx}u_0+\partial_{zz}u_1, \tag{2.29a}$$
$$\mathrm{Re}^*\,z\left(\partial_{xt}u_0+u_0\partial_{xx}u_0+(\partial_x u_0)^2\right)=-\partial_z p_1+z\,\partial_{xxx}u_0+\partial_{zz}w_1, \tag{2.29b}$$
$$\partial_x u_1+\partial_z w_1=0, \tag{2.29c}$$

with boundary conditions at $z=h(x,t)$:

$$\partial_z u_1-\partial_{xx}u_0h_0-4\partial_x h_0\partial_x u_0=0, \tag{2.30a}$$
$$p_1-\phi''(h_0)h_1-2\left(\partial_x u_0(\partial_x h_0)^2+\partial_z w_1-\partial_z u_1\partial_x h_0+h_0\partial_x h_0\partial_{xx}u_0\right)$$
$$-2\partial_x u_0(\partial_x h_0)^2+\partial_{xx}h_1-\frac{3}{2}(\partial_x h_0)^2\partial_{xx}h_0=0, \tag{2.30b}$$
$$\partial_t h_1-w_1+u_0\,\partial_x h_1-u_1\partial_x h_0=0. \tag{2.30c}$$

The boundary condition at $z=0$ are

$$w_1=0 \quad \text{and} \quad \partial_z u_1=\frac{\epsilon^{\alpha-2}}{\beta}u_0. \tag{2.31}$$

The distinguished limit of (2.31) that includes the full influence of the Navier-slip boundary conditions occurs for $\alpha=2$. Integrating (2.29a) with respect to z from $z=0$ to $z=h_0$ and using (2.30a) and $(2.31)_1$, we obtain the equation

$$\mathrm{Re}^*\,(\partial_t u_0+u_0\partial_x u_0)=\frac{4}{h_0}\partial_x(h_0\partial_x u_0)+\partial_x\left(\partial_{xx}h_0-\phi'(h_0)\right)-\frac{u_0}{\beta h_0}. \tag{2.32a}$$

This equation coupled with (2.23c), *i.e.*,

$$\partial_t h_0=-\partial_x\,(h_0u_0)\,, \tag{2.32b}$$

give a closed system for $u_0(x,t), h_0(x,t)$, which we call the strong-slip regime. See also [4] for a different derivation.

We observe that the weak- and the strong-slip regimes represent two distinguished limits in the sense that they represent two scalings which are richer than other slip regimes. While the weak-slip regime (2.15) includes the limiting case $b\to 0$, yielding the popular no-slip lubrication model, the strong-slip regime covers the limiting case $\alpha>2$, yielding the lubrication model for free films; see *e.g.* [15–17]. Note, in this case the last term of Equation (2.32a) is zero. Models containing only the first term of the right-hand side of (2.32a) (often called the Trouton viscosity) are used to describe extensional flow; see *e.g.* [18].

However, there also exists a whole class of regimes intermediate to the two distinguished limits.

2.4. Intermediate slip regimes

To obtain the scalings for the intermediate slip regimes we recall that we identified two velocity scales arising from different scalings of the slip length, *viz.*

$$b=\mathrm{O}(1) \qquad \text{and} \qquad b=\mathrm{O}(\epsilon^{-2}). \tag{2.33}$$

For the intermediate regimes consider the velocity scale, capillary number and Reynolds number to be given by

$$\mathbb{U}=\frac{\sigma\epsilon^{2-\gamma}}{\mu}, \quad \mathrm{Ca}=\epsilon^{2-\gamma}, \quad \mathrm{Re}=\epsilon^{2-\gamma}\mathrm{Re}^*, \tag{2.34}$$

for $-1<\gamma<1$. The governing equations are

$$\epsilon^{3-\gamma}\mathrm{Re}^*\,(\partial_t u+u\partial_x u+w\partial_z u)=-\epsilon^{\gamma+1}\partial_x p+\epsilon^2\partial_{xx}u+\partial_{zz}u, \tag{2.35a}$$

$$\epsilon^{3-\gamma}\mathrm{Re}^*\,(\partial_t w+u\partial_x w+w\partial_z w)=-\epsilon^{\gamma-1}\partial_z p+\epsilon^2\partial_{xx}w+\partial_{zz}w, \tag{2.35b}$$

$$\partial_x u+\partial_z w=0, \tag{2.35c}$$

with boundary conditions at $z=h(x,t)$:

$$\left(\partial_z u+\epsilon^2\partial_x w\right)\left(1-\epsilon^2(\partial_x h)^2\right)+2\epsilon^2\partial_x h\,(\partial_z w-\partial_x u)=0, \tag{2.36a}$$

$$p-\phi'(h)-2\epsilon^{1-\gamma}\frac{\left(1-\epsilon^2(\partial_x h)^2\right)\partial_z w-\partial_x h\left(\partial_z u+\epsilon^2\partial_x w\right)}{1+\epsilon^2(\partial_x h)^2}+\frac{\partial_{xx}h}{\left(1+\epsilon^2(\partial_x h)^2\right)^{3/2}}=0, \tag{2.36b}$$

$$\partial_t h-w+u\,\partial_x h=0, \tag{2.36c}$$

and boundary condition at $z=0$:

$$w=0 \quad \text{and} \quad \partial_z u=\epsilon^\alpha \frac{u}{\beta_{\text{int}}}, \quad \text{where} \quad 0<\alpha<2. \tag{2.37}$$

We now let

$$\begin{aligned} u(x,z,t;\epsilon)&=u_0(x,z,t)+\epsilon^\alpha u_1(x,z,t)+\mathrm{O}(\epsilon^{2\alpha}),\\ w(x,z,t;\epsilon)&=w_0(x,z,t)+\epsilon^\alpha w_1(x,z,t)+\mathrm{O}(\epsilon^{2\alpha})\\ p(x,z,t;\epsilon)&=p_0(x,z,t)+\epsilon^\alpha p_1(x,z,t)+\mathrm{O}(\epsilon^{2\alpha}),\\ h(x,t;\epsilon)&=h_0(x,t)+\epsilon^\alpha h_1(x,t)+\mathrm{O}(\epsilon^{2\alpha}). \end{aligned} \tag{2.38}$$

Obviously, since $-1<\gamma<1$, the leading-order problem is

$$\partial_{zz}u_0=0, \quad \partial_z p_0=0, \quad \partial_x u_0+\partial_z w_0=0, \tag{2.39a,b,c}$$

with boundary conditions at $z=h_0(x,t)$:

$$\partial_z u_0=0, \quad p_0-\phi'(h_0)+\partial_{xx}h_0=0, \quad \partial_t h_0-w_0+u_0\,\partial_x h_0=0, \tag{2.40a,b,c}$$

and boundary conditions at $z=0$:

$$w_0=0 \quad \text{and} \quad \partial_z u_0=0. \tag{2.41}$$

Analogous to the derivation of the strong-slip regime here we find

$$u_0\equiv u_0(x,t), \quad w_0=-z\,\partial_x u_0 \quad \text{and} \quad p_0=-\partial_{xx}h_0+\phi'(h_0)\,. \tag{2.42}$$

The function $u_0(x,t)$ is again found from the next-order correction, with $\alpha=\gamma+1$. We find

$$\partial_z u_1=(h_0-z)\,\partial_x\left(\partial_{xx}h_0-\phi'(h_0)\right), \tag{2.43}$$

which, together with the slip condition at $z=0$,

$$\partial_z u_1=\frac{u_0(x,t)}{\beta_{\text{int}}}, \quad \text{yields} \quad u_0(x,t)=\beta_{\text{int}}\,h_0\partial_x\left(\partial_{xx}h_0-\phi'(h_0)\right). \tag{2.44}$$

Using (2.42) in (2.40c), yields $\partial_t h_0=-\partial_x[h_0u_0]$. Upon inserting $(2.44)_2$, we obtain the lubrication model

$$\partial_t h_0=-\beta_{\text{int}}\,\partial_x\left[h_0^2\,\partial_x\left(\partial_{xx}h_0-\phi'(h_0)\right)\right], \tag{2.45}$$

sometimes also called the 'slip-dominated' lubrication model; see *e.g.* [19–21].

Note that the constant β_{int} can be absorbed by redefining $t\mapsto t/\beta_{\text{int}}$. The intermediate slip model is also obtained as the limiting case of (2.15) divided by b and with time rescaled as $t\mapsto t/b$, for $b\to\infty$ and $h_0=\mathrm{O}(1)$. It is also the limiting case of (2.32) with time rescaled as $t\mapsto t/\beta$ and $u_0\mapsto\beta u_0$, for $\beta\to 0$ and $h_0=\mathrm{O}(1)$.

3. Asymptotics for the dewetting ridge in the no-slip and intermediate slip cases

3.1. The dewetting ridge and the intermolecular potential $\phi(h)$

We make use of these models to study the intermediate asymptotic solutions describing dewetting. Driven by VdW forces, initially small instabilities to uniform thin films will lead to dynamics that closely approximate finite-time point rupture, as described in [22–24]. The presence of a stabilizing short-range contribution to the intermolecular potential prevents complete rupture and determines a lower bound on the film thickness, $h=\nu$, with $0<\nu\ll 1$, where the potential has its minimum. Instead of complete rupture (where $h=0$ is reached), the position of the initial instability becomes the center for a growing circular hole. The displaced fluid collects in a growing ridge (see cross-sectional view in Figure 1) that marks the advancing edge of the dewetting instability. We now describe the structure of this ridge for the lubrication models for the no-slip and the intermediate slip regime from the previous section.

Under ideal conditions, it could be imagined that dry spots could grow indefinitely large. By conservation of mass, the growing holes would shift fluid into the ever-growing rims. In the absence of a large length scale to limit the sizes of these structures, we might expect the motion and growth of the ridges to approach scale-invariant self-similar form. This is the case for the intermediate slip regime. The no-slip case is more delicate and involves logarithmic corrections. In fact, the dynamics of dewetting and ridge growth do not continue indefinitely; for example, secondary instabilities will eventually set in [25, 26]. However, self-similar dynamics for the ridge evolution give an accurate description of the intermediate-time-scale asymptotics.

Note that all of the models derived in the previous section could be analogously generalized to apply to the full three-dimensional problem with the two-dimensional free surface, $z=h(x,y,t)$. For the study of growing axisymmetric dewetting regions, the governing equations can be generalized and written in one-dimensional form in the radial direction in terms of ∂_r derivatives. These equations are non-autonomous in r and solutions will exhibit strong curvature-dependent effects in the early stages of rupture and dewetting. Our study will focus on the intermediate stages of dewetting, when the ridge has propagated outwards sufficiently far, so that the radius of the dewetted region is large compared to the length scale of the ridge and curvature effects can be neglected, so that $\partial_r \approx \partial_x$. Hence, we will consider throughout, the ridge that has formed at the contact-line, as depicted in Figure 3. The hole, *i.e.*, the dewetted area, is behind the ridge, where the film has almost vanished except for a thin residual film of thickness $O(\nu)$, while ahead of the ridge, the film is undisturbed. Far ahead of

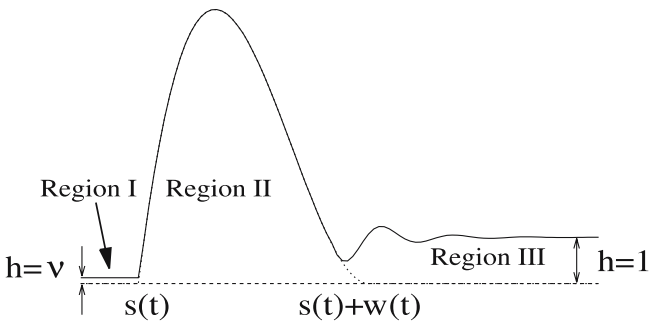

Figure 3. Sketch of the ridge showing the outer region (II) and the two inner regions: the 'dry' inner region (I) and the 'wet' inner region (III).

the ridge we assume that the film thickness is scaled to one, *i.e.*, by choosing the initial film thickness for the normal length scale $\mathbb{H}$. Hence, we have the boundary conditions

$$h \to \nu \quad \text{as} \quad x \to -\infty,$$
$$h \to 1 \quad \text{as} \quad x \to \infty.$$

To describe the potential in terms of a normalized function that does not depend on ν, see also [27], we let

$$\phi(h) = \Phi(h/\nu), \tag{3.1}$$

where $\Phi(\psi)$ with $\psi = h/\nu$ satisfies $\Phi'(1) = 0$ and $\Phi''(1) > 0$. A typical choice for Φ, see [28], is

$$\Phi(\psi) = \frac{1}{8\psi^8} - \frac{1}{2\psi^2}, \tag{3.2}$$

where the second term is a VdW term that drives the dewetting and the first term is a repulsion term that prevents the film thickness from decreasing to zero. In other words, it stabilizes the 'dry' film. More complex compositions of the substrate – *i.e.*, alternating layers of hydrophilic and hydrophobic materials – can introduce further VdW terms $\sim h^{-2}$ with alternating signs. For example, the potential

$$\Phi(\psi) = \frac{a_1}{8\psi^8} - \frac{a_2}{2\psi^2} + \frac{a_3}{(\psi + d)^3}, \tag{3.3a}$$

where a_1, a_2, a_3 and d are positive; see *e.g.* [29]. This combination introduces a third, stabilizing term that makes $\Phi''(\psi) > 0$ for sufficiently large film thickness h. This implies that sufficiently thick flat films are stable against spinodal decomposition.

For specific numerical simulations, we will use either (3.2) or (3.3a) with

$$a_1 = 1{\cdot}014, \quad a_2 = 1{\cdot}014, \quad a_3 = 7{\cdot}465 \quad \text{and} \quad d = 25{\cdot}34; \tag{3.3b}$$

this is simply a rescaled version of the potential that was also used in [21, 25]. (The rescaling was chosen so that the static contact angles for (3.2) and (3.3), *i.e.*, the values for $\Phi(1)$, are equal). Most of the analytical considerations work for fairly general classes of potentials. We will generally assume that Φ has a minimum at $\psi = 1$ and that $\Phi \sim \psi^{-2}$ for $\psi \to \infty$.

3.2. Formulation of the ridge problem

We will go on to show that there are important differences in the structure and dynamics of the ridge in the different models, but first we summarize the shared features. The ridge is a dynamic solution. It connects to the dewetted hole with $h \to \nu$ as it advances into the surrounding uniform film, with $h = 1$. We denote by $x = s(t)$ the position of the former moving interface, *i.e.*, the contact line, while the position of the latter interface will give an effective measure of the width of the ridge, $x = s(t) + w(t)$. The ridge is assumed to be moving forward, $\dot{s}(t) > 0$, corresponding to an expanding hole. The statement of conservation of fluid mass in the ridge consistent with this is

$$\frac{\mathrm{d}}{\mathrm{d}t}\left(\int_{s(t)}^{s(t)+w(t)} h(x,t)\,\mathrm{d}x\right) = (1-\nu)\dot{s}(t) + \dot{w}(t). \tag{3.4}$$

Indeed, as sketched in Figure 3, the analysis of this problem will be broken down into three dominant regions:

(I) $0 \le x < s(t)$ the dewetted hole, $h \sim \nu$,
(II) $s(t) < x < s(t) + w(t)$ the dewetting ridge, $h = h(x, t)$,
(III) $s(t) + w(t) < x$ the surrounding undisturbed film, $h \sim 1$.

In contrast to the analysis in [19], our analysis includes the effect of intermolecular forces. As we will see below, this enforces an additional constraint on the validity of the asymptotic result in the intermediate slip case. The solution will be constructed from matched asymptotic expansions on each of these regions. In our analysis we find it convenient to attack this problem by shifting into the reference frame moving with the contact line:

$$\tilde{x} = x - s(t), \qquad h = h(\tilde{x}, t). \tag{3.5}$$

Then the thin-film equation for the intermediate cases takes the general form,

$$\partial_t h - \dot{s}(t)\partial_{\tilde{x}} h = -\partial_{\tilde{x}} \left[m(h) \partial_{\tilde{x}} \left(\partial_{\tilde{x}\tilde{x}} h - \nu^{-1} \Phi'(h/\nu) \right) \right], \tag{3.6}$$

with the ridge being defined on $0 < \tilde{x} < w(t)$, and where $m(h) = h^3$ denotes the mobility for the no-slip and $m(h) = h^2$ the intermediate slip case, respectively. The boundary conditions are (as stated earlier)

$$h \to \nu \quad \text{as} \quad x \to -\infty, \tag{3.7a}$$
$$h \to 1 \quad \text{as} \quad x \to \infty. \tag{3.7b}$$

As will be shown later, the form of the ridge at the contact line (the matching condition between (I) and (II)) is closely tied to the form of the intermolecular potential function $\Phi(\psi)$.

3.3. Intermediate slip regime

We now consider the evolution of a ridge for the intermediate slip regime, *i.e.*, the lubrication model (2.45). The problem reads, after rescaling by β_{int},

$$\partial_t h - \dot{s}\partial_{\tilde{x}} h + \partial_{\tilde{x}} \left[h^2 \partial_{\tilde{x}} \left(\partial_{\tilde{x}\tilde{x}} h - \nu^{-1} \Phi'(h/\nu) \right) \right] = 0, \tag{3.8}$$

with boundary conditions stated in (3.7a), (3.7b).

Since we are interested in the motion of the ridge at long times after rupture, we introduce a new parameter $\delta \ll 1$ via the stretched time variable $\tau = \delta t$ and investigate the asymptotic behaviour for $\delta \ll 1$, and τ fixed. In the following, we will introduce new spatial variables for each of the three regions that characterize the film profile for the intermediate slip regime. These are region I–III as depicted in Figure 3. The new variables correspond to moving coordinate systems, the origins of which are located at the contact line or the contact line plus the width of the ridge. The contact line position $s(t)$ and the width $w(t)$ both grow in time, *i.e.*, with some power of δ, for fixed τ and $\delta \to 0$. We will therefore assume that $s(t) = \delta^{-\sigma} S(\tau)$ and $w(t) = \delta^{-\omega} W(\tau)$, with $\sigma > \omega > 0$ and $S, W = O(1)$ as $\delta \to 0$.

The resulting problems take the form:
Region (I): dewetted film
We set $\tilde{x}=\nu\xi$ and $h=\nu\psi(\xi,\tau)$. This yields

$$\delta\nu^2\frac{\partial\psi}{\partial\tau}-\delta^{1-\sigma}\nu\dot{S}\frac{\partial\psi}{\partial\xi}+\frac{\partial}{\partial\xi}\left[\psi^2\frac{\partial}{\partial\xi}\left(\frac{\partial^2\psi}{\partial\xi^2}-\Phi'(\psi)\right)\right]=0, \tag{3.9}$$

and the rescaled far-field boundary condition is

$$\psi\to 1 \quad \text{as } \xi\to-\infty. \tag{3.10}$$

Region (II): moving ridge
We set $\tilde{x}=\delta^{-\alpha}X$ and $h=\delta^{-\gamma}H(X,\tau)$, with $\gamma>0$. This yields

$$\delta^{1-\gamma}\frac{\partial H}{\partial\tau}-\delta^{1+\alpha-\gamma-\sigma}\dot{S}\frac{\partial H}{\partial X}+\delta^{2\alpha-2\gamma}\frac{\partial}{\partial X}\left[H^2\frac{\partial}{\partial X}\left(\delta^{2\alpha-\gamma}\frac{\partial^2 H}{\partial X^2}-\nu^{-1}\Phi'(\delta^{-\gamma}H/\nu)\right)\right]=0 \tag{3.11}$$

on $0<X<\delta^{-\omega+\alpha}W(\tau)$.
Region (III): undisturbed film
We set $\tilde{x}=\delta^{-\omega}W(\tau)+\delta^{\mu}z$, while h is not rescaled. This yields

$$\delta\frac{\partial h}{\partial\tau}-\delta^{1-\mu-\sigma}\dot{S}\frac{\partial h}{\partial z}-\delta^{1-\mu-\omega}\dot{W}\frac{\partial h}{\partial z}+\delta^{-4\mu}\frac{\partial}{\partial z}\left[h^2\frac{\partial}{\partial z}\left(\frac{\partial^2 h}{\partial z^2}-\nu^{-1}\delta^{2\mu}\Phi'(h/\nu)\right)\right]=0. \tag{3.12}$$

The far-field condition remains

$$h\to 1 \quad \text{as } z\to\infty. \tag{3.13}$$

We expect the ridge to evolve essentially like a growing self-similar solution within the moving reference frame determined by the contact-line position. For region II, the surface tension should be significant, but the disjoining pressure should be negligible. Consequently, (3.11) suggests the dominant balance

$$1+\alpha-\gamma-\sigma=4\alpha-3\gamma. \tag{3.14}$$

In the appendix it is shown that the leading-order equation for the ridge quasi-statically scales with $\dot{S}(\tau)$ to yield a growing self-similar ridge profile. A consequence of this structure is that the long-time matching behavior to region III determines the fixed self-similar support of the ridge with

$$\omega=\alpha. \tag{3.15}$$

Moreover, the leading-order equation in region I is also quasi-static, we expect the matching between regions I and II to determine a steady finite contact angle (*i.e.*, fixed slope $h_{\tilde{x}}$) which determines the relation

$$\gamma=\alpha. \tag{3.16}$$

From the conservation of mass (3.4), we expect the rate of growth of the ridge to be related to its motion by

$$-\gamma-\omega=-\sigma \quad \text{and hence} \quad \sigma=2\omega. \tag{3.17}$$

A further consequence of the traveling-wave (quasi-static in co-moving frame) balance in Equation (3.12) requires

$$\sigma = 1 + 3\mu \tag{3.18}$$

Consequently we find

$$\gamma = \alpha = \omega = \frac{1}{3}, \qquad \sigma = \frac{2}{3} \quad \text{and} \quad \mu = -\frac{1}{9}. \tag{3.19}$$

Inserting (3.14–3.18) into (3.9–3.13), we get the following leading-order equations in the three regions for $\delta \to 0$:
Region (I):

$$\frac{\partial}{\partial \xi}\left[\psi^2 \frac{\partial}{\partial \xi}\left(\frac{\partial^2 \psi}{\partial \xi^2} - \Phi'(\psi)\right)\right] = 0, \tag{3.20}$$

with the rescaled left boundary condition

$$\psi \to 1 \quad \text{as } \xi \to -\infty. \tag{3.21}$$

Region (II):

$$-\dot{S}\frac{\partial H}{\partial X} + \frac{\partial}{\partial X}\left[H^2 \frac{\partial^3 H}{\partial X^3}\right] = 0. \tag{3.22}$$

Region (III):

$$-\dot{S}\frac{\partial h}{\partial z} + \frac{\partial}{\partial z}\left[h^2 \frac{\partial}{\partial z}\left(\frac{\partial^2 h}{\partial z^2}\right)\right] = 0. \tag{3.23}$$

with the far-field condition on the right

$$h \to 1 \quad \text{as } z \to \infty. \tag{3.24}$$

The disjoining pressure term drops out if $\nu^{-1}\delta^{2\mu}\Phi(h/\nu) \sim \nu^2\delta^{2\mu}h^{-3}$ is small. This imposes a restriction on δ in terms of ν, namely

$$\delta \gg \nu^{-1/\mu} = \nu^9. \tag{3.25}$$

In the appendix we solve above problems and match them. We obtain the following expression for $s(t)$:

$$s(t) \sim \left(\frac{3}{2}\right)^{2/3} M^{1/3}(\tan\theta)^{5/3} t^{2/3}, \tag{3.26}$$

with $M \approx 0{\cdot}0272$, where θ is the contact angle. Note that for fixed τ, the constraint (3.25) imposes an upper asymptotic bound on t, *i.e.*, $t \ll \nu^{-9}$.

We note, that the $t^{2/3}$ behavior was found earlier by experimental and physical arguments in [30–32], asymptotically, neglecting the intermolecular potential in [19] and numerically in [21].

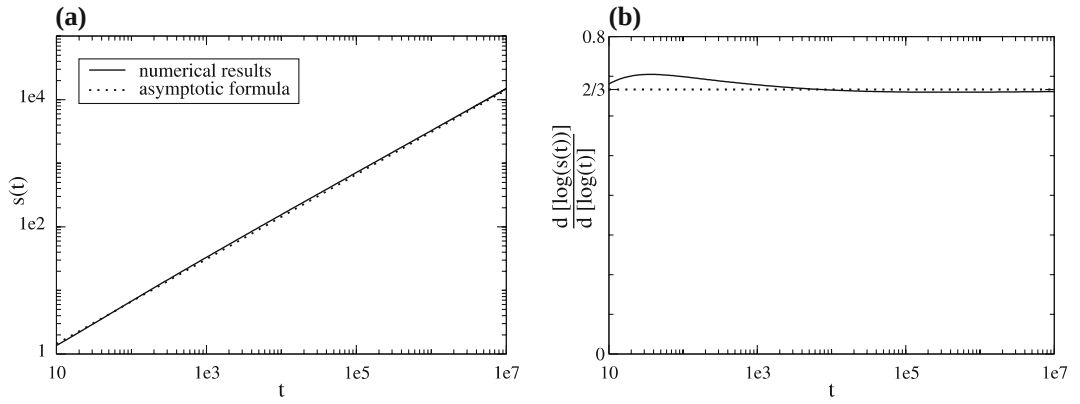

Figure 4. ((a), left) The evolution of the contact line position $s(t)$ for the intermediate slip case with $\nu = 0{\cdot}04$, for the numerical computations and for the asymptotic result (3.26). Figure ((b), right) shows the derivative of $\log(s(t))$ with respect to $\log(t)$.

3.3.1. *Comparison with numerical results*

In Figure 4, we compare the asymptotic formula (3.26) to numerical results for $s(t)$, for $\nu = 0{\cdot}04$ and the intermolecular potential (3.1) using the two-term expression for Φ given in (3.2). We note that the numerical data for the contact line s in this and following plots was normalized by replacing s with $s - \min_t(s(t))$. The comparison shows that the numerical result deviates only slightly from the asymptotic result. In the log-log scaled figure, $s(t)$ tends to a straight line that virtually lies on top of the line for the asymptotic formula (3.26), *i.e.*, the asymptotics captures both the exponent and the prefactor well. Differentiating $\mathrm{d}\log(s)/\mathrm{d}\log(t)$ yields a curve that rapidly asymptotes (after an initial transient overshoot) to a value close to $2/3$. This confirms that $s(t)$ indeed follows a power-law behavior close to $t^{2/3}$ at large times. The asymptotic value for $\mathrm{d}\log(s)/\mathrm{d}\log(t)$ seems to be slightly less than $2/3$, about one percent lower. The value for $\nu = 0{\cdot}04$ is roughly of the same order of magnitude as the deviation.

3.4. No-slip regime

We now consider the evolution of a ridge for the no-slip regime, *i.e.*, the lubrication model (2.15) with the slip length b set to zero.

The problem then reads

$$\partial_t h = -\partial_x \left[h^3 \partial_x \left(\partial_{xx} h - \nu^{-1} \Phi'(h/\nu) \right) \right], \tag{3.27}$$

where we absorbed the factor 3 into the time scaling. It is a widely commented fact (see *e.g.* [19, 20] and references therein) that the spreading law in the no-slip case depends singularly on the precursor thickness, *i.e.*, the time needed for the contact line to travel an O(1) distance increases logarithmically with the regularization parameter. Flitton and King [19] carried out a detailed analysis *via* matched asymptotics for a lubrication model of a dewetting ridge with a sharp contact line, where h is exactly zero and the (static or microscopic) contact angle is explicitly imposed through a boundary condition rather than *via* explicit representation of intermolecular forces. Their model was regularized by including a small slip contribution into the mobility, *i.e.*, using $h^3 + \varepsilon_b h^2$ instead of h^3 as in (3.27). In the limit $\varepsilon_b \to 0$ they obtained the contact-line evolution $s(t)$ including logarithmic corrections in the prefactor.

Flitton and King's derivations can be adapted to the models we use here, and in fact yield the same expressions for $s(t)$, except that the contact angle is set by the intermolecular potential according to (A.4) rather than being imposed as a moving-boundary condition, and the

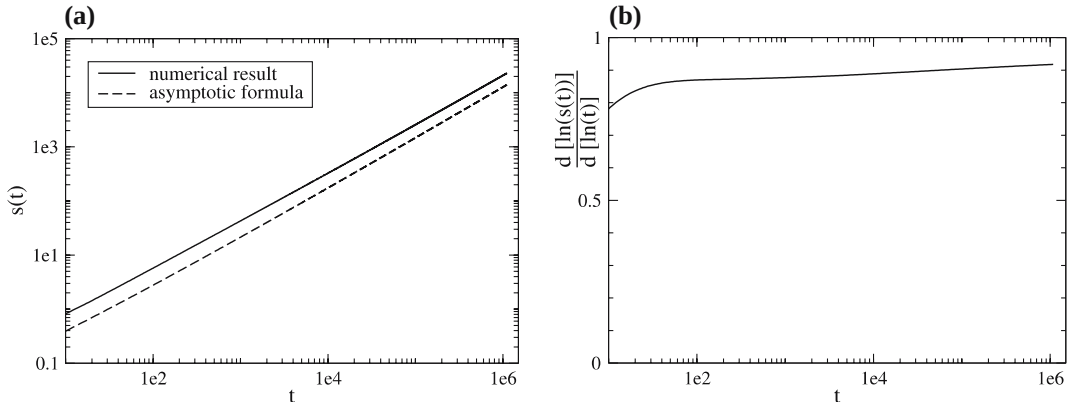

Figure 5. (a) The evolution of the contact line position $s(t)$ for the no-slip case with $\nu = 0{\cdot}04$, comparing the numerical result with the asymptotic expression (3.28). (b) shows the effective dewetting exponent $\mathrm{d}\log(s)/\mathrm{d}\log(t)$ for the numerical result.

residual film thickness ν now takes over the role of ε_b,

$$s(t) \sim \bar{\delta} t \frac{(\tan\theta)^3}{3(\bar{\delta}\log t + 1)} \tag{3.28}$$

where $\bar{\delta} \equiv 1/\ln(1/\nu)$. Similarly, the expression for the width is found to be

$$w(t) \sim \bar{\delta}^{1/2} t^{1/2} \frac{2^{2/3}\tan\theta}{(\bar{\delta}\log t)^{1/6}(1+\bar{\delta}\log t)^{1/3}}. \tag{3.29}$$

3.4.1. *Comparison with numerical results*

We now compare (3.28) with results from numerical simulations of (3.27). A plot of $s(t)$ from a numerical simulation using $\nu = 0{\cdot}04$ and the two-term potential Φ in (3.2) is shown in Figure 5(a), in a log-log plot. The numerical result tends to a straight line with slope one that would correspond to a linear spreading law, $s \sim t$. Closer inspection of Figure 5(b) shows that the effective dewetting exponent $\mathrm{d}\log(s)/\mathrm{d}\log(t)$ appears to tend to one but only very slowly. This is qualitatively consistent with the essentially $t/\log t$-like behavior predicted by (3.28), as $t \to \infty$, which entails $\mathrm{d}\log(s)/\mathrm{d}\log(t) \sim 1 - 1/\log t$, *i.e.*, a logarithmically slow approach of the exponent to one. The presence of logarithmic modifications to a linear law was also observed numerically in [21, 33]. A quantitative comparison of the numerical results and (3.28) in Figure 5(a) shows, however, a deviation of about a factor of two, possibly due to substantial contributions from higher order logarithmic corrections (*i.e.*, higher order terms in $\bar{\delta}$).

4. The dewetting ridge: distinguished limits

4.1. Weak slip

In this section, we track the evolution of the ridge, in particular of the position of the contact-line, in the weak-slip regime. The model (2.15) explicitly contains the slip length b, while the no-slip and the intermediate slip regimes can be recovered from it by letting $b \to 0$ or $b \to \infty$ (after rescaling time with b). Hence, we expect the long-time limits for $s(t)$ to interpolate in some way between the dewetting rates for the no-slip and the intermediate slip regime. In (2.15), the slip length was non-dimensionalized with an arbitrary normal length scale $\mathbb{H}$, but in Section 3 we chose $\mathbb{H}$ to be the initial unperturbed film thickness at $x \to \infty$. Hence, the

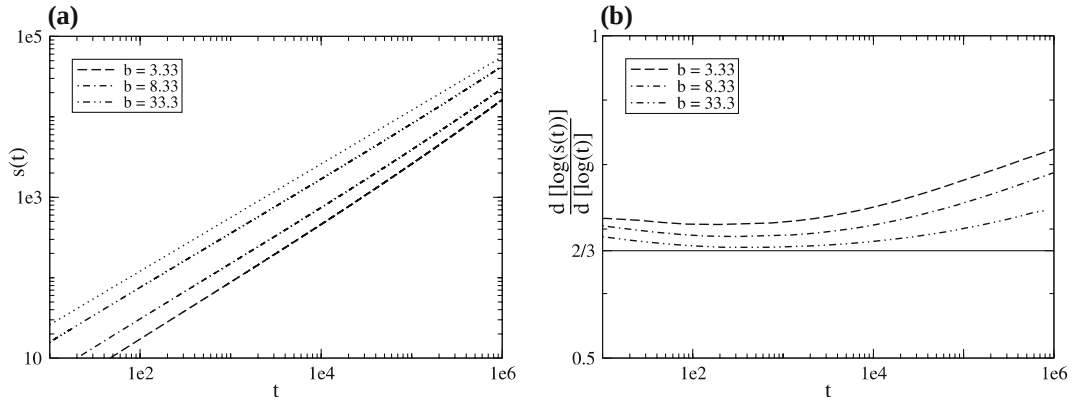

Figure 6. (a) The evolution of the contact line position $s(t)$ for the weak slip model with different slip lengths with $\nu = 0{\cdot}04$, using a log-log scaling of the axes. The thin dotted top line is proportional to $t^{2/3}$ and is included to guide the eye. (b) The derivative of $\log(s(t))$ with respect to $\log(t)$, in a log-linear plot.

non-dimensional b we use here represents the slip length compared to this particular length scale. For the dynamics of the ridge, it seems more reasonable to look at the value of b compared to the height of the ridge, $h_{\max}(t) = \max_x h(x,t)$. Since this grows in time, the effective relative slip length $b/h_{\max}$, decreases, so we expect to see a slow transition from an intermediate-slip to a no-slip like behavior. Of course, in any case, sufficient time must elapse, and a sufficiently large ridge must emerge, before any of the asymptotic rates are valid.

Results from numerical simulations of (2.10a) with $\nu = 0{\cdot}04$ and the two-term potential (3.2) are shown in Figure 6. In Figure 6a, $s(t)$ for several values of the slip are plotted in a log-log graph and are compared with $t^{2/3}$. In particular, the slip lengths that are markedly larger than one, hence allow for an "effective" slip length in the ridge that is larger than one even after the ridge has grown somewhat, tend to fairly straight lines with slope close to the dotted guiding line. However, at later times, in particular for the lower b, the slope of the line becomes larger than the guiding line, indicating an exponent α in the dewetting law t^α that is larger than $2/3$.

We can get a better picture by differentiating the graphs for $\log(s)$ with respect to $\log(t)$. For a pure power t^α law (as for the guiding line), this would yield a constant, *i.e.*, $\mathrm{d}\log(s)/\mathrm{d}\log(t) = \alpha$. One clearly sees, that at later times all $\mathrm{d}\log(s)/\mathrm{d}\log(t)$ are larger than $2/3$ and monotonically growing, which is consistent for a situation with decreasing effective slip. For the two larger slip lengths at least, there is an intermediate period of time, where initial transients have died out, while the "effective" slip length $b/h_{\max} \gg 1$. In this time period, $\mathrm{d}\log(s)/\mathrm{d}\log(t)$ approaches $2/3$ and eventually departs again as the slip length increases further. Furthermore, $\mathrm{d}\log(s)/\mathrm{d}\log(t)$ gets closer to $2/3$ and departs more slowly for larger b.

4.2. Strong slip

4.2.1. *Numerical runs varying β*

In this section, we present numerical results for the evolution of the contact-line for the strong-slip regime (2.32a), (2.32b), for negligible inertia ($\mathrm{Re}^* = 0$). We use the three-term potential (3.3) for Φ, with $\nu = 0{\cdot}04$. As for the weak-slip case, we consider first the limit cases, more precisely, the case when $\beta \to 0$. One easily finds that then the second-order term drops out of (2.32a) and one can solve for u. Inserting the result into (2.32b) yields the PDE for the intermediate slip case (2.45). In the limiting case $\beta \to \infty$ we obtain the model of [16]. The

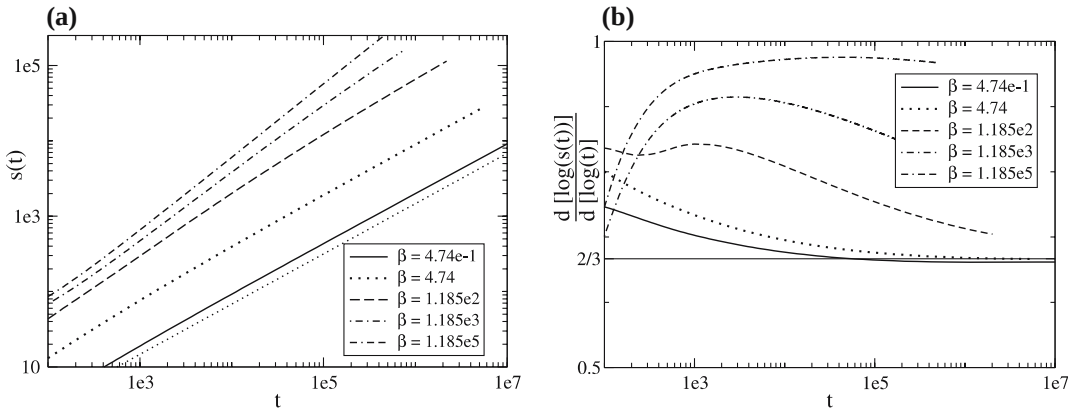

Figure 7. (a) The evolution of the contact line position $s(t)$ for the strong-slip model with different slip lengths β and $\nu = 0{\cdot}04$, and the intermolecular potential (3.3), in a log-log plot The bottom thin dotted line is proportional to $t^{2/3}$ and is included to guide the eye. (b) The derivative of $\log(s(t))$ with respect to $\log(t)$, in a log-linear plot.

values of β we use for our simulations have been non-dimensionalized with the film thickness, but as for the weak-slip case, it seems more relevant for the dynamics of the ridge to consider the effective β that have been rescaled with $h_{\max}$. Since $h_{\max}$ grows in time, the effective β decreases and we must eventually recover the behavior for the $\beta \to 0$ limit, *i.e.*, the dewetting dynamics of the intermediate slip case. Hence, for large times, the slope of the graph t vs. $s(t)$ in a log-log plot must approach a straight line for a $t^{2/3}$ like growth. This is indeed seen in Figure 7(a). Also, one sees that for larger β, it takes longer for the curves to follow the guiding line, while for the largest β they have not yet entered this regime.

Differentiating $\mathrm{d}\log(s)/\mathrm{d}\log(t)$ yields the graphs in Figure 7(b). Here, the approach of 2/3 is even clearer, in particular for the two smallest β. Interestingly, these two lines seem to asymptote to a value that is slightly smaller than 2/3. For the larger β we observe a transition towards higher dewetting rates approaching constant speed (*i.e.*, $\mathrm{d}\log(s)/\mathrm{d}\log(t)$ approaches one) for an intermediate time. This intermediate time grows for increasing β.

4.2.2. *Transitions in shape*

Linear stability analysis about the undisturbed uniform film To gain insight into the structure of the dewetting rim as it propagates into the undisturbed film, we make use of a linearized analysis. We linearize about the base state with respect to infinitesimal perturbations of size δ,

$$h(x,t) \sim 1 + \delta\tilde{h}(x,t), \qquad u(x,t) \sim \delta\tilde{u}(x,t), \qquad \delta \ll 1, \tag{4.1}$$

and obtain the linearized equations,

$$\partial_t\tilde{h} + \partial_x\tilde{u} = 0, \quad \mathrm{Re}^*\partial_t\tilde{u} = 4\partial_{xx}\tilde{u} + \partial_{xxx}\tilde{h} - \phi''(1)\partial_x\tilde{h} - \frac{1}{\beta}\tilde{u} \tag{4.2a,b}$$

To describe the advancing edge of the ridge, it is convenient to shift into a frame of reference co-moving with the ridge, $\xi = x - s(t)$, and seek quasi-stationary solutions in the form of traveling fronts, $\tilde{h} = \tilde{h}(\xi)$. Then, the continuity equation (4.2a) forces $\tilde{u} = \dot{s}\tilde{h}(\xi)$. Inserting this into the momentum equation (4.2b) yields

$$\mathrm{Re}^*\left(\ddot{s}\tilde{h} - \dot{s}^2\frac{\mathrm{d}\tilde{h}}{\mathrm{d}\xi}\right) = 4\dot{s}\frac{\mathrm{d}^2\tilde{h}}{\mathrm{d}\xi^2} + \frac{\mathrm{d}^3\tilde{h}}{\mathrm{d}\xi^3} - \phi''(1)\frac{\mathrm{d}\tilde{h}}{\mathrm{d}\xi} - \frac{\dot{s}}{\beta}\tilde{h}. \tag{4.3}$$

To understand the qualitative forms of the advancing ridge in this equation, we let $\tilde{h}(\xi)=e^{\sigma\xi}$, yielding the characteristic equation

$$\sigma^3+4\dot{s}\sigma^2+\left(\mathrm{Re}^*\dot{s}^2-\varphi\right)\sigma-\left(\mathrm{Re}^*\ddot{s}+\frac{\dot{s}}{\beta}\right)=0, \tag{4.4}$$

where we write $\varphi=\phi''(1)$. Note that in this equation σ depends on t parametrically through $s(t)$.

We will not write out the cumbersome algebraic expressions for the roots of the cubic equation (4.4); however, aspects of the algebra are helpful in understanding the transitions in the ridge structure. Descartes' law of signs shows that there is one positive real root and either two negative or two complex conjugate roots. Physically relevant solutions, with $\tilde{h}(\xi\to\infty)\to 0$, must have $\Re\mathfrak{e}(\sigma)<0$. The change of roots from real to complex conjugate occurs when the discriminant vanishes, equivalently,

$$1-\frac{256}{27}\beta\dot{s}^2-\frac{8}{3}\beta\varphi-\frac{16}{27}\beta^2\varphi^2-\frac{4}{27\dot{s}^2}\beta^2\varphi^3+O(\mathrm{Re}^*)=0 \tag{4.5}$$

for $\mathrm{Re}^*\to 0$. The change in sign can for example be induced by increasing β, which was investigated in [12] and used to explain the experimentally observed transition in dewetting polymer film profiles on various hydrophobic substrate coatings.

From (4.5), we obtain an estimate for the critical ridge speed that separate real-decaying profiles (σ real) from oscillatory profiles (complex conjugate σ) in terms of the slip for weak potentials $\varphi\to 0$:

$$\dot{s}_{\mathrm{crit}}\sim\sqrt{\frac{3}{\beta}}\left[\frac{3}{16}-\frac{1}{4}\beta\varphi\right]. \tag{4.6}$$

Figure 8 shows the resulting line with the contribution from φ. For the potential and parameters used here, $\varphi>0$, so that the line is shifted downwards compared to where it would be for $\varphi=0$, *i.e.*, the contribution from $\varphi>0$ tends to suppress the appearance of oscillations. Recall that for $\nu\to 0$, we have $\varphi\to 0$, so that the contribution from the potential becomes less important. We remark that numerical results for a corresponding linear stability analysis for the Stokes problem are given in [12].

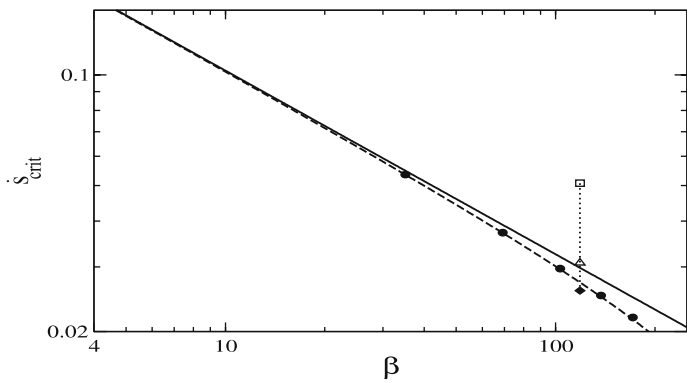

Figure 8. The predicted critical speed (4.6) for the transition in the ridge structure from uniform to oscillatory decay. The data points connected by a thin dotted line correspond to ridge profiles at different times in a numerical simulation of dewetting with $\beta=118{\cdot}5$, see Figures 9 and 10.

Evolution of profiles in time We now use the linearized theory to discuss the evolution of ridge shapes in time. In Section 4.2, we found that as the ridge grows, and achieves a height that is comparable to the slip length, the evolution of the contact-line for the strong-slip resembles that of the intermediate slip case. Here we show that in at least some cases, the ridge profile, too, can change from a monotone decay to the unperturbed film at $x \to \infty$ to having a tail with decaying oscillations. Since we have seen in Figure 7 that the ridge slows down with time for a given fixed β, the speed $\dot{s}$ of the dewetting ridge slowly approaches $\dot{s}_{\text{crit}}$ from above. To illustrate this, we have included the ridge speed for the slip parameter $\beta = 118{\cdot}5$ in Figure 8. The values for $\dot{s}$ were obtained from the numerical solutions at the same times as for the ridge profiles in Figures 9 and 10. Indeed $\dot{s}$ eventually drops below the critical speed. Inspection of the profiles (in Figure 9) for the times corresponding to the top and bottom symbol in Figure 8 indeed reveal a monotonically decaying shape at the earlier time, when $\dot{s}$

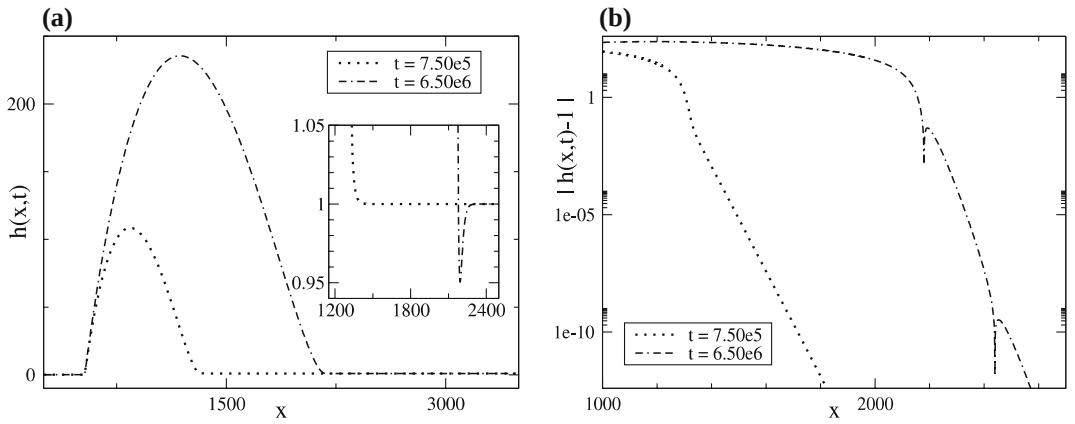

Figure 9. (a) We show the profiles for $\beta = 118{\cdot}5$ and $\nu = 0{\cdot}02$ at two different times, corresponding to the top and bottom symbol in Figure 8 on the dotted line. All profiles are presented in a co-moving frame of reference so the fronts are lined up. The inset shows the portion of the ridge where it connects to the undisturbed film. (b) To better assess whether a minimum and possible further strongly damped oscillations arise, we show a semilog plot of $|h(x,t)-1|$. Zero crossings due to oscillations around the unperturbed film thickness $h = 1$ appear as spikes.

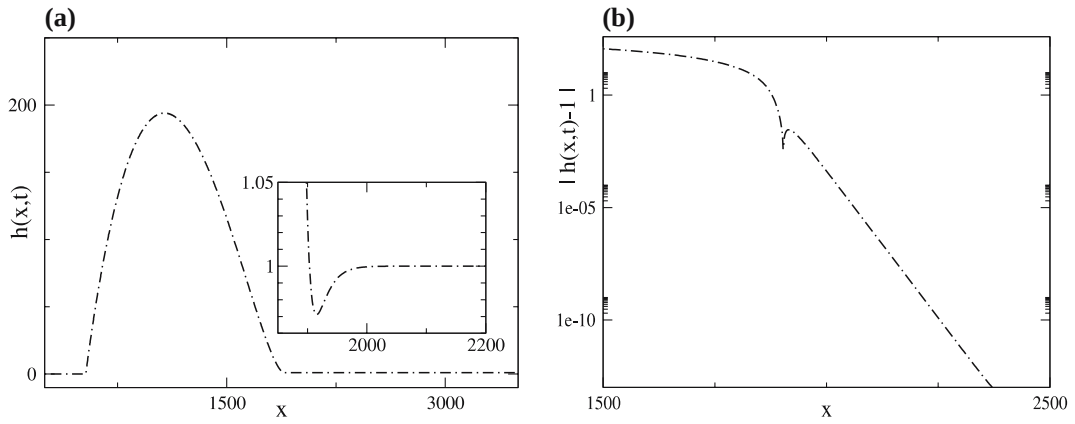

Figure 10. (a) We show the profiles that arise for $\beta = 118{\cdot}5$ and $\nu = 0{\cdot}02$ at time $t = 3{\cdot}75 \times 10^6$, corresponding to the middle symbol on the dotted line in Figure 8. The inset shows the portion of the ridge where it connects to the undisturbed film. A slight undershoot is just visible. (b) To better assess whether a minimum and possible further oscillations arise, we show a semilog of $|h(x,t)-1|$. There is only one spike indicating a single undershoot but no further oscillations.

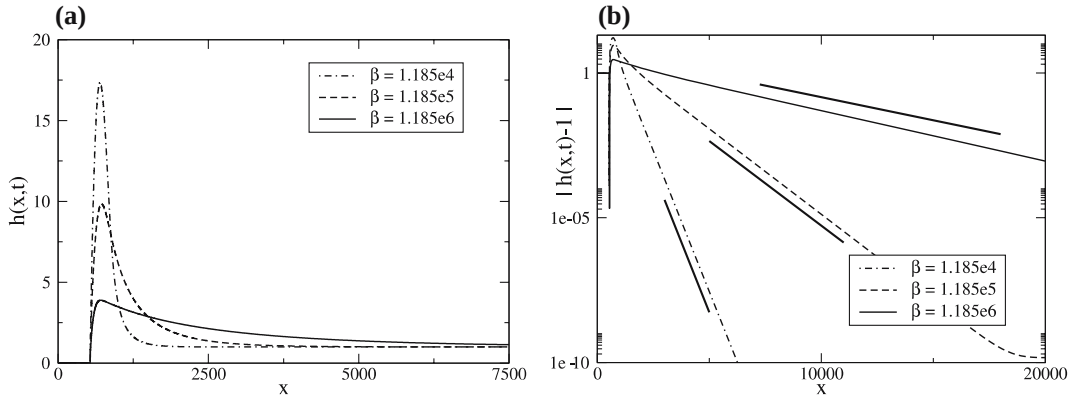

Figure 11. (a) Ridge profiles for very large values of β, for dimensionless time $t = 10^4$. (b) Semilog plot of $|h(x,t)-1|$, cut off at some small non-negative value. The short solid lines are proportional to $\exp(\sigma x)$ where σ is the negative real eigenvalue from (4.4) with the smallest modulus. All profiles in (a) and (b) are for the potential (3.1), (3.3) and $\nu = 0{\cdot}02$.

is still larger than $\dot{s}_{\text{crit}}$, and decaying oscillations for the later t, where $\dot{s} < \dot{s}_{\text{crit}}$. The appearance of two spikes in Figure 9(b) means that at least the first two of the infinite number of intersections of h and h_∞ could be detected in the numerical data. For the intermediate time corresponding to the middle symbol in Figure 8 which still lies above $\dot{s}_{\text{crit}}$ but is quite close to it, the profile has a single undershoot but no further oscillations (Figure 10); only one spike arises in Figure 10(b). Such a single undershoot can arise from two real negative eigenvalues in (4.4) in particular as they tend to a double eigenvalue as $\dot{s}$ approaches $\dot{s}_{\text{crit}}$.

Very large slip parameter β As we have seen in Figure 7(b), for very large β the dewetting rates approach an almost constant speed. The corresponding profiles in these cases are shown in Figure 11(a). The profiles are taken at a fixed dimensionless time but it turns out that the front positions for the ridges are also similar. One clearly sees the asymmetric profile with a steep front on the 'dry' side and an exponential decay on the 'wet' side . This asymmetry becomes more pronounced as the exponential decay rate decreases as we make β larger. To illustrate the effect more clearly, Figure 11(b) shows a semilog plot of the profiles minus the unperturbed film thickness. The slopes of the lines agree with the negative real eigenvalue of with the smallest modulus of (4.4). Interestingly, dewetting ridges with similar profiles have been observed experimentally for highly elastic and long-chain polymer films [34, 35].

5. Conclusions

In this article we derived a family of lubrication models from the Navier-Stokes equations together with a Navier-slip condition having a range of orders of magnitude for the slip-length parameter. As the orders of magnitude of this parameter increases from zero, the flow field changes from parabolic to plug flow.

We obtained five asymptotic regimes, two of them, the weak- and the strong-slip regime, represent distinguished limits. Both regimes have as a limiting case the intermediate slip regime, while the no-slip and the free-slip regime is obtained by taking the slip-length parameter to zero in the weak and by letting it go to infinity in the strong-slip regime, respectively.

In applications, these obtained models have shown to be able to explain various challenging physical phenomena concerned with dewetting thin films, such as the finger instability near the

contact line of the dewetting rim, see *e.g.* [21, 25, 36], where the intermediate slip regime was investigated, or the shape of the dewetting rim, changing from damped oscillatory to monotone decay towards the undisturbed film, as the slip-length increases; see also [12].

We used matched asymptotic solutions to derive the dewetting rates of the ridge for the no-slip and intermediate slip cases and complemented those with numerical solutions to cover the rates for the distinguished limit cases. The weak- and strong-slip regimes show a tendency towards a linear dewetting law for the front position, while in the intermediate regime, we get a $t^{2/3}$ law. Interestingly, our asymptotic analysis predicts that, upon including the intermolecular potential, the validity of the intermediate slip regime is limited by the thickness of the remaining film in the dewetted region, defined by the minimum of the intermolecular potential.

Additionally, we found that the profiles of the rims are fairly symmetrical in the no-slip and weak-slip regime, but, on the other hand, become very asymmetric in the strong-slip regime for very large values of the slip parameter. Interestingly, the latter problem has been attributed in the physics literature to viscoelastic effects [37] or shear thinning [38], while here the properties of the liquid in the bulk are purely Newtonian and we show that these morphological changes are brought about by changing a single parameter associated with the liquid/solid interface, *i.e.*, the Navier-slip length. Moreover, we show that for large slip lengths, the rim profiles initially show monotonic decay towards the undisturbed film, but an oscillatory decay sets in as the rim becomes larger over time. We could predict this transition also by a linear stability analysis.

In a separate article [39] we have studied the corresponding three-dimensional flow problems for the no-slip and intermediate slip regimes and investigated the stability of the contact line against spanwise perturbations both numerically for the lubrication models and asymptotically for the corresponding sharp-interface models, derived there. Presently we investigate the situation for the strong-slip model where the inertial terms are included and how it may change the dynamical structure.

Appendix. Matching the dewetting ridge problem

In this appendix we carry out the details involved in solving and matching together the problems involved in the intermediate-slip regime, (3.20)–(3.24):

Region (I):

Integrating the leading-order problem

$$\frac{\partial}{\partial\xi}\left[\psi^2\frac{\partial}{\partial\xi}\left(\frac{\partial^2\psi}{\partial\xi^2}-\Phi'(\psi)\right)\right]=0,\qquad \psi\to 1\quad \text{as } \xi\to-\infty \tag{A.1}$$

in the usual fashion, we obtain the first order ODE

$$\psi_\xi=\sqrt{2(\Phi(\psi)-\Phi(1))}. \tag{A.2}$$

For our interest in matching to this solution, we only need the behaviour of ψ for $\xi\to\infty$. From (A.2), the asymptotic behavior of ψ can be written as

$$\psi(\xi)\sim\begin{cases}\xi\tan\theta & \xi\to\infty,\\ 1 & \xi\to-\infty,\end{cases}\qquad \text{with}\quad \tan\theta=\sqrt{-2\Phi(1)}. \tag{A.3}$$

Rescaling into outer variables yields

$$H\sim X\tan\theta. \tag{A.4}$$

Region (II):
The leading-order problem is

$$-\dot{S}\frac{\partial H}{\partial X}+\frac{\partial}{\partial X}\left[H^2\frac{\partial}{\partial X}\left(\frac{\partial^2 H}{\partial X^2}\right)\right]=0. \tag{A.5}$$

The disjoining pressure drops out, since the dominant behaviour typically is $\Phi'(\psi)\sim\psi^{-3}$ hence $\nu^{-1}\delta^{3\mu}\Phi'(\delta^{3\mu}h/\nu)\sim\nu^2\delta^{-6\mu}h^{-3}$, where $\mu<0$ as we will see below. The leading-order problem can be integrated once,

$$-\dot{S}H+H^2\frac{\partial^3 H}{\partial X^3}=K_1, \tag{A.6}$$

with a yet unknown constant of integration. We can argue as follows that K_1 must be zero. Matching H to the two inner layers requires that $H\to 0$ for finite X on both sides. However, it has been found [40] that the ODE (A.6) with H^2 in front of the third-order term and $K_1\neq 0$ does not permit solutions that touch down on both sides, *i.e.*, have and 'advancing' and a 'receding' front. Setting $K_1=0$ yields

$$H\frac{\partial^3 H}{\partial X^3}=\dot{S}, \tag{A.7}$$

with a lower power of H in front of H_{XXX}. For this ODE, solutions with two fronts that touch down are permitted.
Region (III):
The leading-order problem in this region is

$$-\dot{S}\frac{\partial h}{\partial z}+\frac{\partial}{\partial z}\left[h^2\frac{\partial}{\partial z}\left(\frac{\partial^2 h}{\partial z^2}\right)\right]=0,\quad \text{with } h\to 1\quad \text{as } z\to\infty. \tag{A.8}$$

The disjoining pressure term drops out if $\nu^{-1}\delta^{2\mu}\Phi(h/\nu)\sim\nu^2\delta^{2\mu}h^{-3}$ is small. For negative μ, this imposes a restriction on δ in terms of ν, namely

$$\delta\gg\nu^{-1/\mu}. \tag{A.9}$$

Integrating the leading-order problem for region III once yields

$$-\dot{S}(h-1)+h^2\frac{\partial^3 h}{\partial z^3}=0. \tag{A.10}$$

Rescaling $z=\zeta/\dot{S}^{1/3}$ yields

$$h_{\zeta\zeta\zeta}=\frac{1}{h^2}(h-1). \tag{A.11}$$

A power-law *ansatz* for the behavior at $\zeta\to-\infty$ suggests (in accordance with King and Bowen [20, p. 328, Equation (2.18)] that

$$h(\zeta)\sim 2(2/3)^{1/2}(-\zeta)^{3/2}, \tag{A.12}$$

hence

$$h(z)\sim 2(2/3)^{1/2}\dot{S}^{1/2}(-z)^{3/2}. \tag{A.13}$$

In outer coordinates, this expansion reads

$$H\sim 2(2/3)^{1/2}\dot{S}^{1/2}(\delta^{\alpha-\omega}W-X)^{3/2}.$$

At this point it is useful to fix ω. In outer scales, the ridge extends from $X=0$ to $X=\delta^{\alpha-\omega}W$ with W an order one quantity in δ. Since we expect a finite width of the ridge (that is, in fact, constant to leading order δ), the only reasonable choice is setting

$$\omega=\alpha \tag{A.14}$$

and we obtain

$$H\sim 2(2/3)^{1/2}\dot{S}^{1/2}(W-X)^{3/2}. \tag{A.15}$$

Note, together with (3.14), (3.16)–(3.18) the condition (A.14) yields (3.19).

Matching the outer problem to the inner ones means that the we must solve the ODE (A.7) subject to the boundary conditions (A.4) and (A.15) at $X=0$ and $X=W$, respectively. We can remove $\dot{S}$ and $\tan\theta$ from this problem by rescaling appropriately,

$$X=(\tan^2\theta/\dot{S})\tilde{x},\quad h=(\tan^3\theta/\dot{S})\varphi,\quad W=(\tan^2\theta/\dot{S})\,d, \tag{A.16}$$

to get

$$\varphi\varphi_{\tilde{x}\tilde{x}\tilde{x}}=1, \tag{A.17}$$

$$\varphi\sim\tilde{x}\quad\text{at}\quad\tilde{x}\to 0, \tag{A.18}$$

$$\varphi\sim 2(2/3)^{1/2}(d-\tilde{x})^{3/2}\quad\text{at}\quad\tilde{x}\to d. \tag{A.19}$$

Boatto *et al.* [40] convert this problem into finding a co-dimension one orbit of a second-order ODE system connecting equilibria, hence generically solutions will exists but only for isolated values of the remaining free parameter d. In fact, one can integrate the ODE (A.17) once to get

$$\varphi\varphi_{\tilde{x}\tilde{x}}-\frac{1}{2}\varphi_{\tilde{x}}^2=\tilde{x}+K_2. \tag{A.20}$$

From the boundary conditions (A.18), (A.19), we get $K_2=-1/2$ and $d+K_2=0$, respectively, so that we have

$$d=1/2. \tag{A.21}$$

Finally, we obtain from the mass balance for the leading-order outer solution

$$\int_0^W H\,\mathrm{d}X=S, \tag{A.22}$$

rescaled with (A.16), the relation

$$\frac{\tan^3\theta}{\dot{S}}\frac{\tan^2\theta}{\dot{S}}M(\varphi)=S,\qquad\text{where}\quad M(\varphi):=\int_0^{1/2}\varphi\,\mathrm{d}\tilde{x}. \tag{A.23}$$

Recall that φ is the solution of (A.17–A.19) with $d=1/2$, and $\tan\theta$ was defined in (A.3). Integrating this ODE for $\dot{S}$ yields

$$S(\tau)=\left(\frac{3}{2}\right)^{2/3}M^{1/3}(\tan\theta)^{5/3}\tau^{2/3}. \tag{A.24}$$

Using $t=\tau/\delta$ and $s(t)=\delta^{-\sigma}S(\tau)$, and noting that we had found $\sigma=2/3$ in (3.19), we obtain

$$s(t)=\left(\frac{3}{2}\right)^{2/3}M^{1/3}(\tan\theta)^{5/3}t^{2/3}. \tag{A.25}$$

For M, we numerically obtain the value $M\approx 0{\cdot}0272$.

Acknowledgements

AM acknowledges support via DFG grant MU 1626/3-1 and by the DFG research center MATHEON, Berlin. TW is grateful for the hospitality of WIAS and HU and was supported by NSF grants #0244498 and #0239125.

References

1. A. Oron, S.H. Davis, and S.G. Bankoff, Long-scale evolution of thin liquid films. *Rev. Mod. Phys*. 69 (1997) 931–980.
2. A.L. Bertozzi and M.P. Brenner, Linear stability and transient growth in driven contact lines. *Phys. Fluids* 9 (1997) 530–539.
3. D.E. Kataoka and S.M. Troian, A theoretical study of instabilities at the advancing front of thermally driven coating films. *J. Coll. Interf. Sci*. 192 (1997) 350–362.
4. P.G. López, S.G. Bankoff and M.J. Miksis, Non-isothermal spreading of a thin liquid film on an inclined plane. *J. Fluid Mech*. 11 (1996) 1–39.
5. A. Münch and B.A. Wagner, Numerical and asymptotic results on the linear stability of a thin film spreading down a slope of small inclination. *Eur. J. Appl. Math*. 10 (1999) 297–318.
6. J.L. Barrat and L. Bocquet, Large slip effect at a nonwetting fluid-solid interface. *Phys. Rev. Lett*. 82 (1999) 4671–4674.
7. F. Brochard-Wyart, P.-G. de Gennes, H. Hervert and C. Redon, Wetting and slippage of polymer melts on semi-ideal surfaces. *Langmuir* 10 (1994) 1566–1572.
8. N.V. Priezjev and S.M. Troian, Molecular origin and dynamic behavior of slip in sheared polymer films. *Phys. Rev. Lett*. 92 (2004) 018302.
9. A. Sharma and J. Mittal, Instability of thin liquid films by density variations: a new mechanism that mimics spinodal dewetting. *Phys. Rev. Lett*. 89 (2002) 186101.
10. V. Shenoy and A. Sharma, Dewetting of glassy polymer films. *Phys. Rev. Lett*. 88 (2002) 236101.
11. E. Lauga, M. Brenner and H. Stone, Microfluidics: The no-slip boundary condition. *Handbook of Experimental Fluid Dynamics*, Springer. Preprint available at: http://arxiv.org/pdf/cond-mat/0501557 (2005), (to appear).
12. R. Fetzer, K. Jacobs, A. Münch, B. Wagner and T. Witelski, New slip regimes and the shape of dewetting thin films. *Phys. Rev. Lett*. 95 (2005) 127801.
13. S.M. Troian, E. Herbolzheimer, S.A. Safran and J.F. Joanny, Fingering instabilities of driven spreading films. *Europhys. Lett*. 10 (1989) 25–30.
14. K. Kargupta, A. Sharma and R. Khanna, Instability, dynamics and morphology of thin slipping films. *Langmuir* 20 (2004) 244–253.
15. M.P. Brenner and D. Gueyffier, On the bursting of viscous films. *Phys. Fluids* 11 (1999) 737–739.
16. T. Erneux and S.H. Davis, Nonlinear rupture of free films. *Phys. Fluids* 5 (1993) 1117.
17. G. Sünderhauf, H. Raszillier and F. Durst, The retraction of the edge of a planar liquid sheet. *Phys. Fluids* 14 (2002) 198–208.
18. J. Eggers, Nonlinear dynamics and breakup of free-surface flows. *Rev. Mod. Phys*. 69 (1997) 865–929.
19. J.C. Flitton and J.R. King, Surface-tension-driven dewetting of Newtonian and power-law fluids. *J. Engng. Math*. 50 (2004) 241–266.
20. J.R. King and M. Bowen, Moving boundary problems and non-uniqueness for the thin film equation. *Eur. J. Appl. Math*. 12 (2001) 321–356.
21. A. Münch, Dewetting rates of thin liquid films. *J. Phys.: Condensed Matter* 17 (2005) S309–S318.
22. T.P. Witelski and A.J. Bernoff, Dynamics of three-dimensional thin film rupture. *Physica D* 147 (2000) 155–176.
23. M.B. Williams and S.H. Davis, Nonlinear theory of film rupture. *J. Coll. Interf. Sci*. 90 (1982) 220–228.
24. W.W. Zhang and J.R. Lister, Similarity solutions for van der waals rupture of a thin film on a solid substrate. *Phys. Fluids* 11 (1999) 2454–2462.
25. A. Münch and B. Wagner, Contact-line instability of dewetting thin films. *Physica D* (2005) accepted.
26. C. Neto, K. Jacobs, R. Seemann, R. Blossey, J. Becker and G. Grün, Satellite hole formation during dewetting: experiment and simulation. *J. Phys.: Condensed Matter* 15 (2003) 3355–3366.
27. K. Glasner and T. Witelski, Coarsening dynamics of dewetting films. *Phys. Rev. E* 67 (2003) 016302.

28. R. Seemann, S. Herminghaus, and K. Jacobs, Dewetting patterns and molecular forces: a reconciliation. *Phys. Rev. Lett*. 86 (2001) 5534–5537.
29. R. Seemann, S. Herminghaus and K. Jacobs, Gaining control of pattern formation of dewetting films. *J. Phys.: Condensed Matter* 13 (2001) 4925–4938.
30. G. Reiter and R. Khanna, Kinetics of autophobic dewetting of polymer films. *Langmuir* 16 (2000) 6351–6357.
31. C. Redon, J.B. Brzoska and F. Brochard-Wyart, Dewetting and slippage of microscopic polymer films. *Macromolecules* 27 (1994) 468–471.
32. F. Brochard-Wyart, G. Debregeas, R. Fondecave and P. Martin, Dewetting of supported viscoelastic polymer films: birth of rims. *Macromolecules* 30 (1997) 1211–1213.
33. A. Ghatak, R. Khanna and A. Sharma, Dynamics and morphology of holes in dewetting of thin films. *J. Coll. Interf. Sci*. 212 (1999) 483–494.
34. R. Seemann, S. Herminghaus and K. Jacobs, Shape of a liquid front upon dewetting. *Phys. Rev. Lett*. 87 (2001) 196101.
35. G. Reiter, Dewetting of highly elastic thin polymer films. *Phys. Rev. Lett*. 87 (2001) 186101.
36. A. Münch, Fingering instability in dewetting films induced by slippage. MATHEON preprint number 123 (2004).
37. S. Herminghaus, R. Seemann and K. Jacobs, Generic morphologies of viscoelastic dewetting fronts. *Phys. Rev. Lett*. 89 (2002) 56101.
38. F. Saulnier, E. Raphaël and P.G. de Gennes, Dewetting of thin film polymers. *Phys. Rev. E.* 66 (2002) 061607.
39. J.R. King, A. Münch and B. Wagner, Stability of a ridge. *Nonlinearity* (2005) submitted.
40. S. Boatto, L.P. Kadanoff and P. Olla, Traveling-wave solutions to thin-film equations. *Phys. Rev. E* 48 (1993) 4423–4431.